

Characterizing the radiative effect of rain using a global ensemble of cloud resolving simulations

P. G. Hill¹, J. C. Chiu^{1,2}, R. P. Allan^{1,3}, J.-D. Chern^{4,5}

¹Department of Meteorology, University of Reading, Reading, UK

²Colorado State University, Fort Collins, USA

³National Centre for Earth Observation, Reading, UK

⁴NASA Goddard Space Flight Center, Greenbelt, Maryland, USA

⁵University of Maryland, Maryland, USA

Key Points:

- We provide the first global assessment of the radiative effect of rain.
- In the global mean, the radiative effect of rain is negligibly small.
- At smaller spatial scales and shorter timescales, rain radiative effects exceeding 10 W m^{-2} do occur, but infrequently.

Corresponding author: Peter Hill, p.g.hill@reading.ac.uk

Abstract

The effect of rain on radiative fluxes and heating rates is a process that is neglected in most of the large scale atmospheric models used for weather forecasting or climate prediction. Yet, to our knowledge, the magnitude of the resulting radiative bias remains unquantified. This study aims to quantify the rain radiative effect (RRE) at a range of temporal and spatial scales, as a step towards determining whether the radiation schemes in these models should include rain. Using offline radiative transfer calculations with input from an ensemble of cloud resolving model simulations, we find that rain has a negligible effect on global mean radiative fluxes (less than 0.2 W m^{-2}). Weekly mean RREs at specific locations may be larger (less than 4 W m^{-2}). At the finest temporal and spatial resolutions, the RRE can occasionally be much larger again (greater than 100 W m^{-2}), but values exceeding 10 W m^{-2} occur in less than 0.1% of cases. Using detailed analysis of case studies we demonstrate that the magnitude and direction of the RRE depend on the rain water path, its vertical location with respect to cloud and, for longwave radiation, the temperature at which it occurs. Large RREs generally only occur when the rain water path is large and the cloud water path is small. These cases are infrequent and intermittent. As the RREs are generally small, we conclude that this missing process is unlikely to be important for large scale atmospheric models.

1 Introduction

Accurate simulation of the atmospheric radiation budget is crucial for modeling both the general circulation and the effect of anthropogenic emissions on climate. Nevertheless, comparison with satellite and surface irradiance observations shows that many large scale atmospheric models (LSAMs) have persistent large shortwave (SW) and longwave (LW) radiation errors, with typical zonal mean errors of 10 W m^{-2} at the top of atmosphere [e.g. *Calisto et al.*, 2014; *Dolinar et al.*, 2014], and typical global mean errors of 10 W m^{-2} at the surface [e.g. *Ma et al.*, 2014; *Wild et al.*, 2014]. Most of these errors are thought to be due to deficiencies in modeled cloud and aerosol, but errors can also result from neglecting physical processes in the radiation schemes. One particular bias that persists in many LSAM radiation schemes is to neglect the radiative impacts of precipitating hydrometeors, including snow, rain, hail and graupel. *Li et al.* [2013] hypothesized that this may be partly responsible for the particularly large (greater than 20 W m^{-2}) climate model radiation biases that are evident in strongly precipitating regions.

45 However, on a global scale, the magnitude of the radiative effect of precipitating hy-
46 drometeors remains uncertain. It is certainly smaller than that of suspended hydrometeors
47 (i.e. clouds), because precipitating hydrometeors occur less frequently and (as precipitating
48 particles are larger) cause less extinction per unit mass than suspended hydrometeors. Yet
49 the primary reason that the radiative effects of precipitating hydrometeors are not accounted
50 for in LSAMs is that historically, they have not been treated explicitly by the microphysics
51 and consequently their mass mixing ratios have not been available for input to the radiation
52 schemes. However, cloud resolving models (CRMs), which explicitly represent the micro-
53 physics of precipitating hydrometeors, usually also account for their radiative effects [e.g.
54 *Fu et al.*, 1995; *Petch*, 1998; *Jiang and Cotton*, 2000; *Phillips and Donner*, 2006; *Tao et al.*,
55 2014]. Moreover, there is a growing body of evidence to suggest that neglecting precipitating
56 ice (snow) in radiative transfer calculations may lead to non-negligible biases in LSAMs [e.g.
57 *Li et al.*, 2014a,b, 2016a,b; *Chen et al.*, 2018]. As a result, *Li et al.* [2016c] suggested that
58 the persistent radiation biases seen across many LSAMs may partly result from neglecting
59 the radiative effects of precipitating hydrometeors.

60 Compared to snow [e.g. *Waliser et al.*, 2011], the radiative impacts of neglecting rain
61 are less well documented. Previous assessments of the radiative effect of rain are rare, and
62 have been based on a limited number of test cases with some contradictory conclusions.
63 Based on radiative transfer calculations for a two-dimensional CRM simulation of 24 hours
64 of a tropical mesoscale convective system, *Xu and Randall* [1995] found that the impact of
65 rain on the SW transmission and albedo was less than 0.002 and concluded that the radia-
66 tive effects of rain were negligible. In contrast, based on idealized cloud and rain profiles
67 *Savijärvi et al.* [1997] found that rain increased the total column SW absorption by approx-
68 imately 10 % for a heavily precipitating cumulonimbus with rain drops present throughout
69 the depth of the cloud. Moreover, *Savijärvi and Räisänen* [1998] found that for an optically
70 thick cloud with base at 3 km, including rain below the cloud base in their radiative transfer
71 calculations could increase the downwelling LW irradiance at the surface by up to 24 W m⁻².
72 However, they acknowledged that in reality the mean effect was likely to be much smaller
73 due to larger water vapor values below cloud base than in their calculations. To our knowl-
74 edge, these are the only existing attempts to quantify the broadband radiative effect of rain;
75 the global radiative effect of rain remains unquantified.

76 The aim of this study is thus to advance upon this limited but potentially important
77 past research by calculating the rain radiative effect for a realistic set of atmospheric profiles

78 encompassing the whole globe. Using these calculations, we aim to quantify and explain the
79 direct radiative effects of rain across a range of temporal and spatial scales. This is necessary
80 to determine whether including rain in LSAM radiative transfer calculations warrants further
81 investigation. Our estimate of the rain radiative effect (RRE) is based on detailed radiative
82 transfer calculations using the SOCRATES (Suite Of Community RAdiative Transfer codes
83 based on *Edwards and Slingo* [1996]) radiation scheme, and a global ensemble of CRM data
84 taken from a state-of-the-art Goddard multiscale modeling framework (GMMF) simulation.

85 The following section details the GMMF simulation output that is used as input to our
86 radiative transfer calculations and the radiative transfer scheme used to perform these calcu-
87 lations, including new parametrizations of the single scattering properties of rain. Section 3
88 describes the radiative effect of rain at a range of scales, from global mean to instantaneous in-
89 dividual CRM profiles. Section 4 outlines the factors that control the radiative effect of rain.
90 We conclude this article with a summary of the results and a brief discussion of the implica-
91 tions for large scale atmospheric models.

92 **2 Methods**

93 **2.1 Goddard multiscale modeling framework simulation**

94 To properly assess the global radiative effect of rain, simultaneous profiles of both pre-
95 cipitating and suspended hydrometeors are required, including both light and heavy precip-
96 itation, over both land and ocean. Unfortunately, no existing observations are able to fulfill
97 all the criteria required. For example, the 17-year satellite-based Tropical Rainfall Measur-
98 ing Mission (TRMM) radar provided vertical profiles of rainwater content [*Iguchi et al.*,
99 2000] but not suspended hydrometeors. Products based on the CloudSat cloud profiling
100 radar instrument include both suspended and precipitating hydrometeors profiles over ocean,
101 but no retrievals of rain profiles exist over land [*L'Ecuyer and Stephens*, 2002; *Lebsock and*
102 *L'Ecuyer*, 2011]. In the absence of suitable observational data, we rely on detailed simula-
103 tions. Global models and reanalyses can provide comprehensive global datasets, but lack
104 the small-scale hydrometeor data required to accurately calculate the rain radiative effect.
105 Cloud resolving models provide the high-resolution vertically resolved structure of both sus-
106 pended and precipitating hydrometeors required for our radiative transfer calculations, but
107 lack global coverage. In order to attain both global coverage and small-scale hydrometeor
108 data, we use output from a multiscale modeling framework (MMF; also known as “super-

109 parametrization”) simulation where a global atmospheric model is run with a cloud resolving
110 model embedded within each gridbox. This framework provides a global ensemble of cloud
111 resolving model data and has previously proved useful for analyzing the radiative effect of
112 other processes that are not usually included in LSAMs, such as subgrid-scale cloud radia-
113 tion interactions [Cole *et al.*, 2005a] and three dimensional effects [Cole *et al.*, 2005b].

114 For this study, we use data from a GMMF simulation that couples the Goddard Earth
115 Observing System (GEOS; a global atmospheric model) with the Goddard Cumulus Ensem-
116 ble Model (GCE; a cloud-resolving model). Specifically, the GMMF simulation referred
117 to as the L2014 experiment in Chern *et al.* [2016], was used. Of the four simulations anal-
118 ysed in that study, the L2014 simulation had the most complete cloud microphysical scheme.
119 The L2014 also generally had amongst the smallest errors compared to all the observations
120 considered in that study, including top of atmosphere (TOA) radiation, cloud fractions and
121 hydrometeor water paths. The simulation was run from 1 December 2006 to 31 December
122 2008, with weekly sea surface temperatures from the NOAA optimum interpolation dataset
123 [Reynolds *et al.*, 2007] and initial conditions based on the ERA-Interim reanalysis [Dee
124 *et al.*, 2011]. The GEOS model was run with a horizontal resolution of 2 degrees latitude
125 and 2.5 degrees in longitude, and 48 layers in the vertical. The GCE cloud-resolving model
126 (CRM) embedded within each GEOS grid box was run in two dimensions, with 32 columns
127 each 4 km wide and 44 layers. We refer to the GCE columns as CRM profiles hereafter.

128 All hydrometeors are handled by the CRM, which uses a single moment bulk micro-
129 physics scheme [Lang *et al.*, 2014; Tao *et al.*, 2016]. Six hydrometeors species are repre-
130 sented: cloud liquid, rain, cloud ice, snow, graupel and hail. The hydrometeor species are
131 treated as horizontally homogeneous within the CRM profiles (i.e. there is no fractional
132 occurrence of the hydrometeors within the CRM profiles). Radiation calculations in the
133 GMMF are also handled by the CRM and all six hydrometeor species are included in the
134 radiation calculations [e.g. Tao *et al.*, 2003]. Further details of the GMMF setup for this sim-
135 ulation can be found in Chern *et al.* [2016].

136 Our analysis is based on hourly output from two weeks of GMMF simulated data, one
137 week each in Boreal Winter (1-7 January 2007) and Boreal Summer (1-7 July 2007). This
138 corresponds to more than 140 million CRM profiles. Figures 1 and 2a,b show the mean area
139 fractions of the six hydrometeors species in these CRM profiles. A number of key features
140 are found in these figures. Firstly, all species generally have peak fractions in the tropics cor-

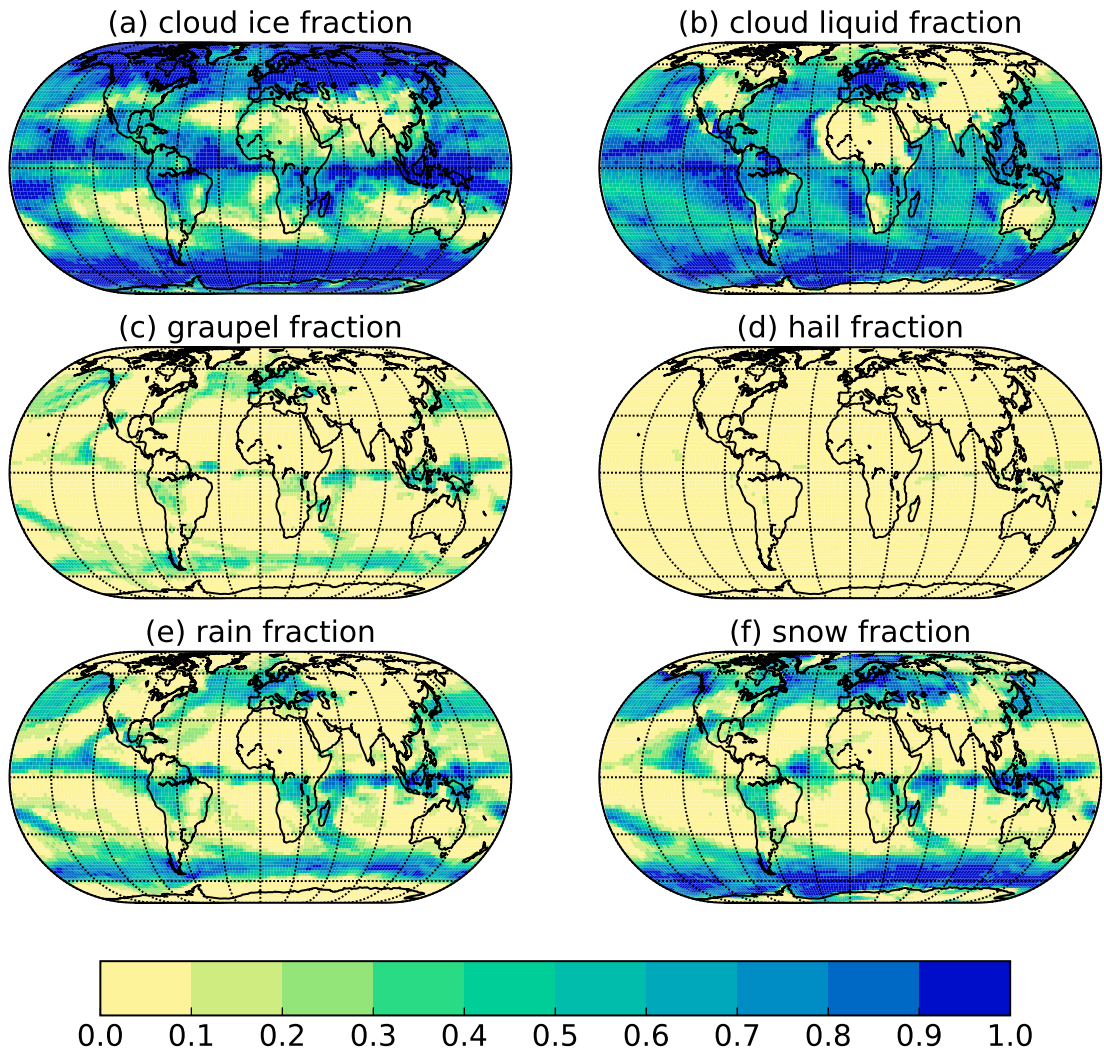
141 responding to the Intertropical Convergence Zone (ITCZ), and at $\sim 50^\circ$ north and south cor-
142 responding to mid-latitude storm tracks, with minima in the subtropics corresponding to the
143 subsidence zones. Secondly, the suspended hydrometers (i.e. cloud liquid and cloud ice) oc-
144 cur more frequently than the precipitating hydrometeors. Among precipitating hydrometeors,
145 snow has the largest area fraction, while the rain fraction is similar to snow at low latitudes
146 but smaller at high latitudes. The graupel fraction is generally less than half that of rain and
147 the hail fraction is smaller still. Finally, comparison between Figures 2a and 2b shows the
148 expected interseasonal differences. The ITCZ is located further north during the boreal sum-
149 mer, while ice fractions increase at the expense of liquid in high latitudes during the winter.

150 Figures 2c and 2d show the zonal mean water paths. Similarly to the fractions, all
151 species have water path maxima in the ITCZ and mid-latitude storm tracks, and minima
152 in the subsidence zones. The interseasonal differences in the water path values also follow
153 a similar pattern to those for the hydrometeor fractions. However, water path values in the
154 ITCZ are much larger than those in the mid-latitude storm tracks, particularly for rain.

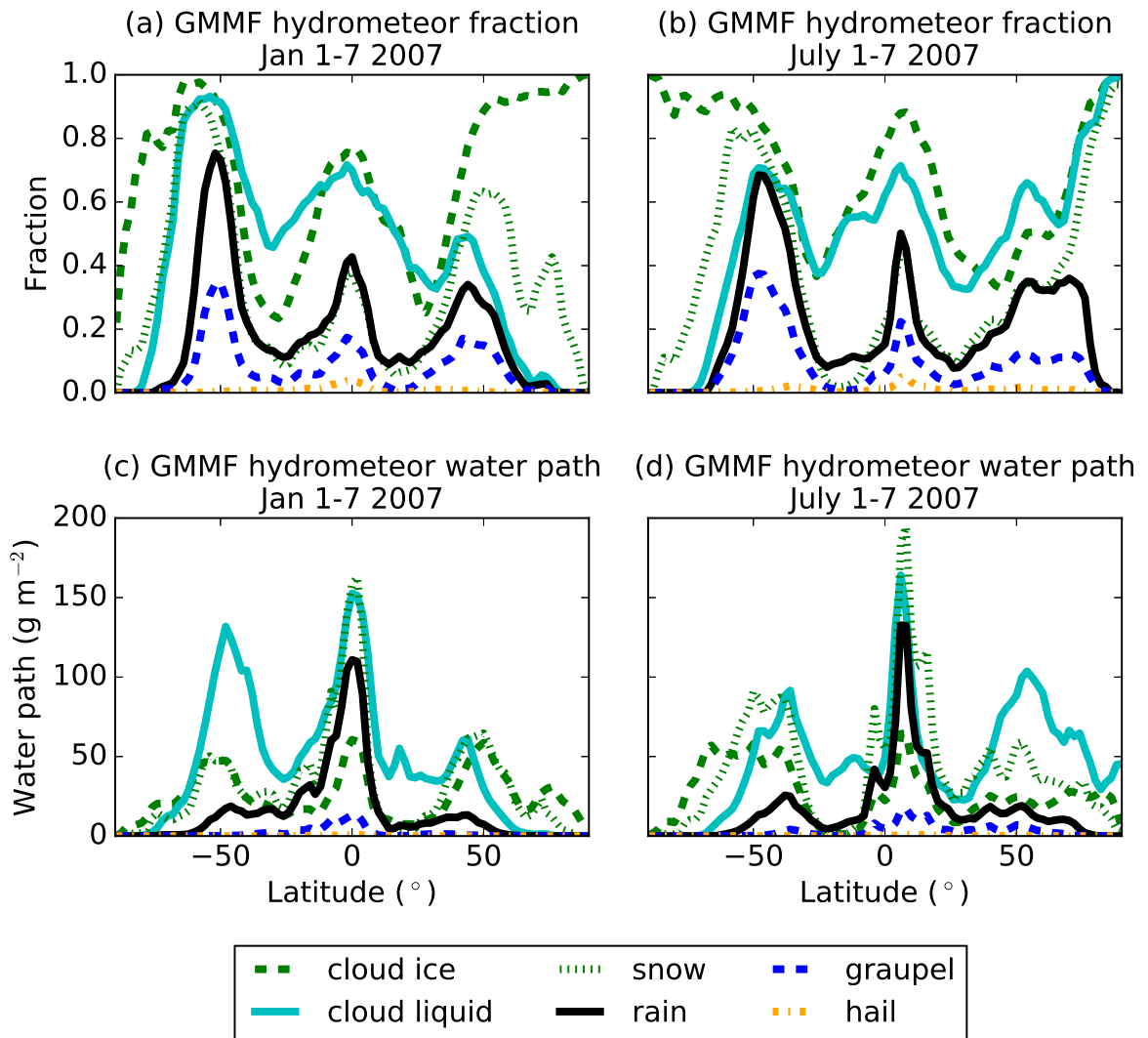
160 Clearly, the credibility of our estimates of the RRE strongly depend on the realism of
161 this GMMF hydrometeor data. *Chern et al.* [2016] showed that ice water content in this sim-
162 ulation is within the observational uncertainty. The realism of the other hydrometeors in the
163 GMMF is harder to assess due to the aforementioned lack of reliable global precipitating
164 hydrometeor datasets. The GMMF is thought to underestimate the global mean rain water
165 path, while overestimating surface precipitation in the tropics [*Chern et al.*, 2016], which is
166 a common problem for MMF simulations [*Tao et al.*, 2009]. Consequently we might expect
167 to underestimate the RRE globally, while overestimating it in the tropics. Nevertheless, for
168 reasons of physical consistency, if the radiative effect of rain in a model is significant, then
169 the radiative effect of rain should be included in that model, irrespective of whether it is rep-
170 resentative of the true radiative effect of rain. Consequently, even if the GMMF derived RRE
171 is imperfect, it remains useful as an example of the magnitude of the RRE in a LSAM.

172 **2.2 Representation of hydrometeors in the SOCRATES radiative transfer scheme**

173 GMMF atmospheric profiles are used as input to offline radiative transfer calculations
174 using the SOCRATES radiative transfer scheme [*Edwards and Slingo*, 1996]. This is a flex-
175 ible one-dimensional radiative transfer scheme that is employed in both numerical weather
176 prediction (NWP) and climate models. Our calculations are based on the two-stream approx-



155 **Figure 1.** Distributions of mean fractions of the hydrometeor species in the GMMF simulation for January
156 1-7 2007, based on a layer mass mixing ratio threshold of 10^{-7} kg kg⁻¹.



157 **Figure 2.** Zonal mean fractions (a,b) and water paths (c,d) of the six hydrometeor species in the GMMF
 158 simulation for (a,c) January 1-7 and (b,d) July 1-7, 2007, based on a layer mass mixing ratio threshold of 10^{-7}
 159 kg kg^{-1} .

177 imation and use the correlated-k method to treat gaseous absorption. We use 21 k-terms in
178 the SW spread between 6 spectral bands between 200 nm and 10 μm . We use 47 k-terms in
179 the LW spread between 9 spectral bands between 3.3 μm and 1 cm. Mixing ratios for the six
180 hydrometeor species and water vapor, pressure, temperature and surface albedos are based on
181 GMMF output. Mass mixing ratios of oxygen, carbon dioxide, methane and dinitrogen ox-
182 ide are set to horizontally and vertically constant values. The LW surface emissivity is set to
183 one, globally. Hydrometeor mass mixing ratios below $1.0 \times 10^{-7} \text{ kg kg}^{-1}$ are set to zero. We
184 calculate radiative fluxes independently for each CRM profile. Aerosols are not included.

185 Radiative transfer calculations through hydrometeor layers require knowledge of the
186 single scattering properties for each spectral band and each hydrometeors species, specif-
187 ically the mass extinction coefficient β , the single scattering albedo ω , and the asymme-
188 try factor g . The current version of SOCRATES accounts for the radiative effects of cloud
189 liquid, cloud ice and snow, but not other species. The single scattering properties of cloud
190 droplets are calculated from the cloud liquid mass mixing ratio and effective radius pro-
191 vided by the GMMF, using the parametrization described by Edwards and Slingo [1996].
192 The cloud droplet effective radius in the GMMF varies from 8 - 14 μm , depending on tem-
193 perature and surface type. Suspended cloud ice and precipitating snow are treated as a single
194 ice category in our calculations, with single scattering properties calculated from the ice plus
195 snow mass mixing ratios and temperature provided by the GMMF, using the parametrization
196 described by *Baran et al.* [2013]. This parametrization is based on an ensemble of ice crys-
197 tal shapes ranging from simple pristine ice crystals to complex snow aggregates [*Baran and*
198 *Labonnote*, 2007] and does not discriminate between ice and snow. Consequently, we are un-
199 able to calculate a snow radiative effect and for the rest of this paper, we use “ice” to refer to
200 the combination of both suspended ice (i.e., cloud ice) and precipitating ice (i.e., snow).

201 Since parametrizations of the single scattering properties of rain, graupel and hail are
202 not included in SOCRATES, new parametrizations were derived for these species. We shall
203 describe this parametrization process in detail for rain. Rain droplets can be reasonably ap-
204 proximated as spheres [e.g. *Beard et al.*, 2010], and Mie theory is applied to calculate the
205 single scattering properties. We assumed a water density of 1000 kg m^{-3} for rain and the re-
206 fractive index was taken from *Hale and Querry* [1973] in the SW and *Downing and Williams*
207 [1975] in the LW. To ensure that the new parametrization is consistent with the rain mass
208 mixing ratios and temperatures predicted by the CRM, we take the range of mass mixing ra-
209 tios predicted by the CRM (1.0×10^{-7} to 5.0 kg kg^{-1}) and divide this into 250 evenly spaced

bins. For each bin, we randomly sample 8 CRM points with mass mixing ratios within the bin limits. For each point, we use the rain mass mixing ratio and corresponding temperature sampled from the GMMF to generate a distribution of rain droplet sizes across 1000 bins, following the same hydrometeor mass mixing ratio and temperature dependent *Marshall and Palmer* [1948] distribution as the CRM microphysics scheme. Mie calculations are performed on this distribution to derive the rain single scattering properties for each combination of rain mass mixing ratio and temperature, for wavelengths between 0.2 μm and 2 cm.

Once the Mie calculations are complete, we average in wavelength space to calculate mean single scattering properties for each point for each of the SOCRATES spectral bands. In the SW, this averaging uses weighting by the incident TOA irradiance for each wavelength. In the LW, the averaging uses weighting by the thermal source function. For each SOCRATES spectral band, this leaves us with 2000 combinations (8 points per bin times 250 bins) of mass mixing ratio (q) and effective radius (r_e , calculated from the size distribution of rain droplets) corresponding to 2000 values of β , ω , and g . A least squares method is then used to parametrize this dataset using the simple equations proposed by *Slingo and Schrecker* [1982]. Further details of these parametrizations are available in the Appendix.

Despite the irregular shape of graupel and hail, we also use Mie theory to calculate their optical properties. *Tang et al.* [2017] demonstrated this to be a reasonable approximation. The optical properties of graupel and hail are parametrized in a manner analogous to those for rain, with two major differences. First, the refractive index of ice is based on the review of *Warren* [1984], except for between 1.4 and 2.5 μm , where the imaginary part of the refractive index is based on the more recent and accurate measurements of *Kou et al.* [1993]. Secondly, we assume ice densities of 300 kg m^{-3} and 900 kg m^{-3} for graupel and hail, respectively.

Figure 3 compares the newly parametrized extinction and single scattering albedo of rain, graupel and hail to those of cloud liquid and ice at wavelengths between 1.19 and 2.38 μm , one of the SOCRATES spectral bands. Recall that the Marshall-Palmer size distributions used in the CRM depend on the mass of hydrometeor and temperature (section 2.1). For the purpose of this comparison, effective radii for these three species are calculated using these same CRM size distributions with a temperature of 273.15 K. This results in effective radii of 116 – 920 μm for rain, 300 μm – 2.4 mm for hail, and 1.8 – 3.9 mm for graupel, for

242 the mass mixing ratio range given in Figure 3, with larger effective radii for larger mass mix-
 243 ing ratios. For liquid, we use the same temperature of 273.15 K and assume the cloud is over
 244 land, resulting in a cloud droplet effective radius of 8 μm . For ice, the parametrization de-
 245 scribed in *Baran et al.* [2013] was designed to avoid the concept of effective radii and has
 246 a stronger temperature dependence. We therefore plot the ice single scattering properties at
 247 two temperatures, 173.15 K and 273.15 K, which demonstrates the range of possible values
 248 from this parametrization.

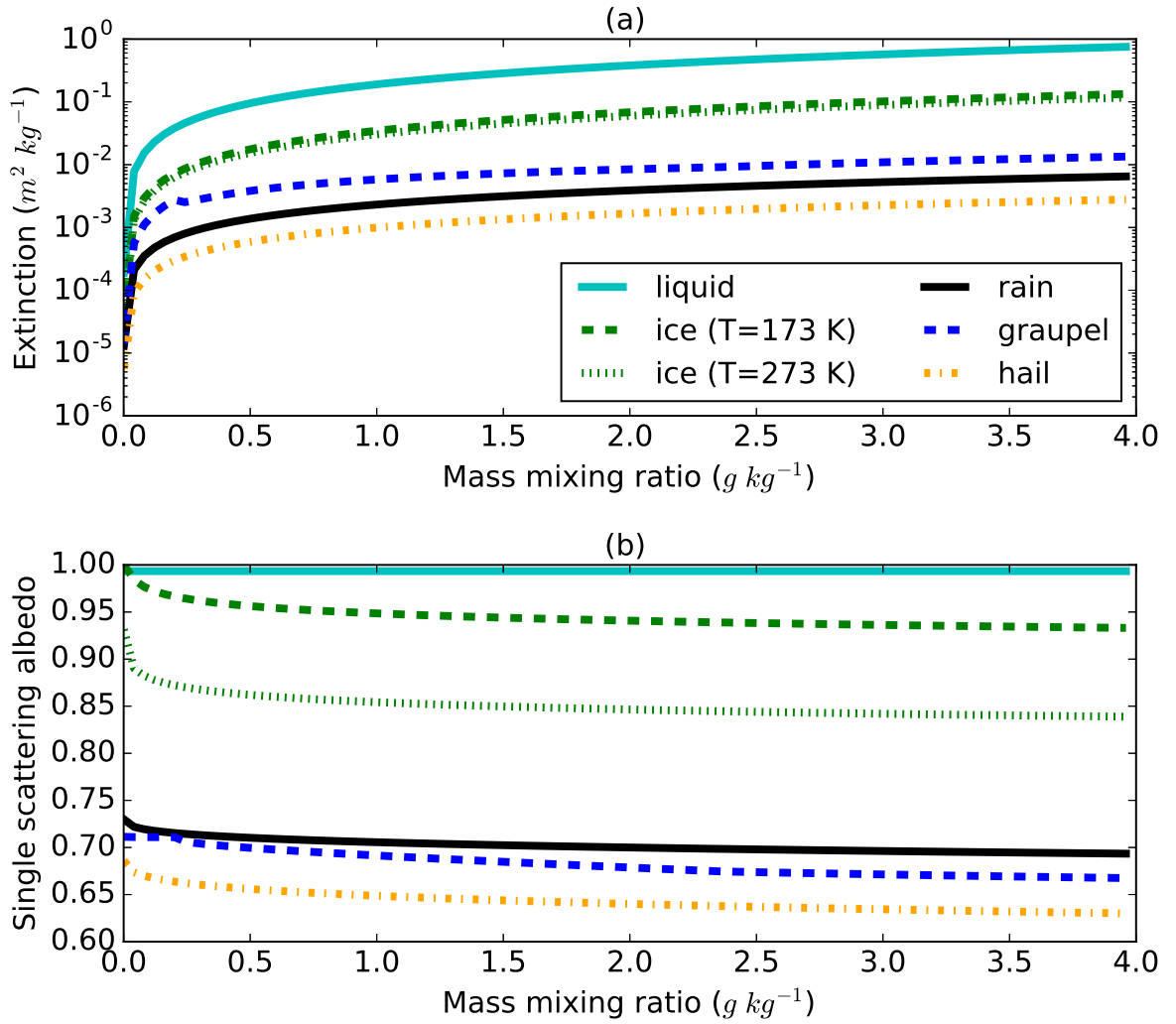
249 As shown in Figure 3a, the extinction due to rain, graupel and hail is at least an order
 250 of magnitude smaller than for the same mass of ice or liquid. Although the extinction for
 251 each hydrometeor species varies with wavelength, the relative magnitude of the extinction
 252 for each hydrometeor species in the other spectral bands is similar to that shown here. Addi-
 253 tionally, Figure 3b shows that the parametrized single scattering albedo for rain, graupel and
 254 hail is much smaller than that for liquid cloud and ice. This is because the single scattering
 255 albedo generally decreases as the particle size increases [e.g. *Slingo and Schrecker*, 1982],
 256 and rain, graupel and hail particles are larger on average than cloud droplets, ice crystals and
 257 snow aggregates. Again, the relative magnitude of the single scattering albedo for each hy-
 258 drometeor species in the other spectral bands is similar to that shown in Figure 3a.

261 **3 The radiative effect of rain**

262 To assess the radiative effect of rain, we examine the difference between two experi-
 263 ments. The first experiment, denoted as ‘all_hydro’ is our control experiment, including all
 264 six hydrometeor species in our radiative transfer calculations. In the second experiment, de-
 265 noted as ‘no_rain’, we exclude rain by setting its mixing ratio to zero in the radiation scheme
 266 for all grid points. For completeness, we also calculate graupel and hail radiative effects us-
 267 ing additional ‘no_graupel’ and ‘no_hail’ experiments that exclude graupel and hail, respec-
 268 tively. Finally, to put these results in context, we perform a clear-sky experiment, excluding
 269 all suspended and precipitating hydrometeors, which is used to calculate the total hydrome-
 270 teor radiative effect.

271 From these experiments, the radiative effect of each precipitating hydrometeor species
 272 is given by:

$$RE = (I_{all}^{\downarrow} - I_{all}^{\uparrow}) - (I_{noj}^{\downarrow} - I_{noj}^{\uparrow}) \quad (1)$$



259 **Figure 3.** Parametrized single scattering properties for the different hydrometeor species as a function of
 260 their mass mixing ratio, for a shortwave spectral band at 1.19–2.38 μm wavelength used in SOCRATES.

273 where I^\downarrow and I^\uparrow denote the downwelling and upwelling irradiance, respectively. The sub-
 274 script “all” denotes irradiances from the “all_hydro” experiment, while “no j” denotes ir-
 275 radiances from the experiment that excludes the j-hydrometeor species, such as no_rain,
 276 no_graupel or no_hail. Using rain as an example, the rain radiative effect (RRE) can be cal-
 277 culated by:

$$RRE = (I_{all}^\downarrow - I_{all}^\uparrow) - (I_{no_rain}^\downarrow - I_{no_rain}^\uparrow) \quad (2)$$

278 This definition is analogous to the commonly used cloud radiative effect (CRE), where clear-
 279 sky is a ‘no_cloud’ calculation. This definition is applied to both TOA and surface radiative
 280 effects, while the in-atmosphere radiative effect is calculated as the difference between the
 281 TOA and surface radiative effects and provides a measure of the vertically integrated change
 282 in absorption by the atmosphere and hence heating of the atmosphere. In practice, rain may
 283 cause both heating and cooling at different heights within the same atmospheric column.
 284 Consequently, the vertically integrated heating may have a smaller magnitude than the heat-
 285 ing of individual layers within a column.

286 3.1 Global mean rain radiative effect

287 Using equation 1, we derived the global, area-averaged mean radiative effects of rain,
 288 graupel, hail and all hydrometeors (Table 1). The mean cloud radiative effect (i.e. all hy-
 289 drometeors) is included to provide context for the radiative effects of the precipitating hy-
 290 drometeors. The RRE has the same signs as CRE in all SW and LW quantities listed in Table
 291 1, but with much smaller magnitudes as expected from Figures 2 and 3. At the TOA and the
 292 surface, absorption and emission of LW radiation by rain increases the net downward LW
 293 irradiance, while reflection and absorption of SW radiation reduces the net downward SW
 294 irradiance. The opposing effects on LW and SW net irradiances lead to a smaller total net
 295 RRE, which has the same sign as the CRE at the TOA and in-atmosphere. At the surface,
 296 where the net CRE is negative, the net RRE is positive due to rain occurring closer to the sur-
 297 face than clouds, leading to relatively large LW warming of the surface. Since the RRE at the
 298 TOA and the surface is at least an order of magnitude smaller than the current observational
 299 irradiance uncertainty [e.g. *Stephens et al.*, 2012], and the total net radiative effect is much
 300 smaller than CRE, we conclude that the contribution of rain to the *global mean* radiation
 301 budget is negligible.

302 Graupel and hail global mean radiative effects are much smaller than the RRE, which
 303 is not surprising considering that graupel and hail occur much less frequently than rain (as
 304 shown in Figure 2). Hail has the same sign SW and LW radiative effects as rain and cloud,
 305 but the graupel radiative effect has the opposite sign for the SW at the TOA and the LW in
 306 the atmosphere. The change of the sign in the SW is because graupel absorbs sunlight that
 307 would otherwise be reflected by liquid or ice clouds. The change of the sign in the LW is
 308 because graupel commonly occurs high enough that the TOA LW radiative effect is much
 309 larger than the surface LW radiative effect, much like ice clouds [e.g. *Hong et al.*, 2016]. As
 310 the graupel and hail radiative effects are much smaller than rain, we shall focus on rain in the
 311 rest of this article.

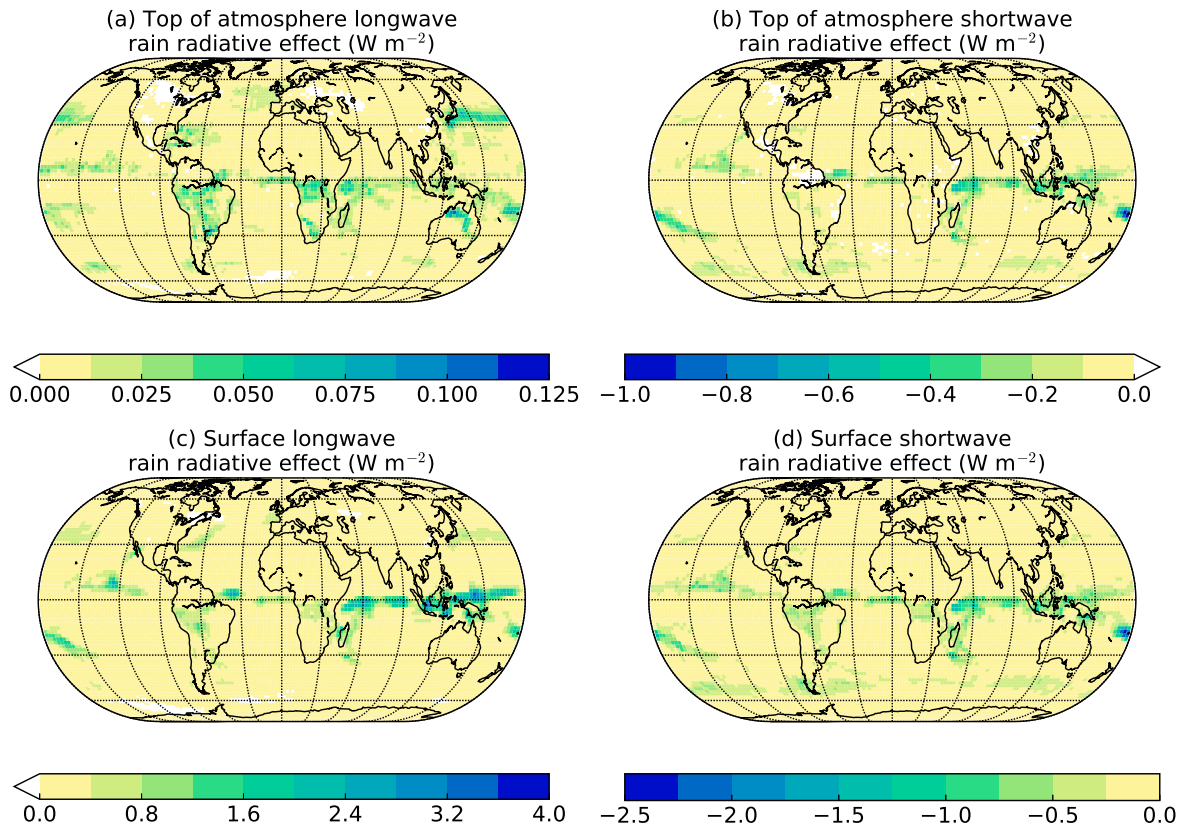
Radiative effect (W m^{-2})	All hydrometeors	Rain	Graupel	Hail
LW TOA	2.0×10^1	6.7×10^{-3}	5.9×10^{-3}	1.1×10^{-5}
SW TOA	-4.4×10^1	-3.4×10^{-2}	3.2×10^{-3}	-7.0×10^{-6}
Net TOA	-2.4×10^1	-2.7×10^{-2}	9.1×10^{-3}	3.9×10^{-6}
LW surface	2.5×10^1	1.6×10^{-1}	1.8×10^{-3}	1.6×10^{-5}
SW surface	-4.8×10^1	-1.0×10^{-1}	-1.3×10^{-2}	-7.7×10^{-5}
Net surface	-2.3×10^1	6.4×10^{-2}	-1.1×10^{-2}	-6.1×10^{-5}
LW in atmosphere	-5.7×10^0	-1.6×10^{-1}	4.2×10^{-3}	-5.4×10^{-6}
SW in atmosphere	4.0×10^0	6.6×10^{-2}	1.6×10^{-2}	7.0×10^{-5}
Net in atmosphere	-1.7×10^0	-9.1×10^{-2}	2.0×10^{-2}	6.5×10^{-5}

312 **Table 1.** Area weighted global mean radiative effect of rain, graupel, hail and cloud (all hydrometeors)
 313 derived from two weeks (one winter, one summer) of hourly GMMF data.

314 **3.2 Spatial distribution of the rain radiative effect**

315 The distribution of RRE correlates strongly with the occurrence of rain. The largest
 316 LW RRE at the TOA occurs in the ITCZ and storm tracks (Figure 4a), where rain occurs
 317 most frequently (see Figures 1 and 2). This pattern is repeated in the LW RRE at the surface
 318 (Figure 4c) and in the SW (Figures 4b and 4d), but with different magnitudes. At the surface,
 319 the LW RRE is much larger than at the TOA, up to 4 W m^{-2} in the ITCZ where the rainwater
 320 paths are largest (Figure 2c). In the SW, the RRE at the surface is about twice as large as the

321 RRE at the TOA, due to absorption of sunlight by rain. At both the TOA and the surface, the
 322 SW RRE is larger in the ITCZ than in the mid-latitude storm tracks, again due to larger rain-
 323 water paths in the ITCZ. Similar patterns are also found in the RREs for 1 – 7 July 2007 (not
 324 shown), but with the ITCZ and associated RRE shifted slightly further north (cf. Figure 2),
 325 with increased SW RRE in the northern hemisphere and decreased SW RRE in the southern
 326 hemisphere due to the seasonal changes in TOA incoming SW irradiance.



327 **Figure 4.** Mean radiative effect (W m^{-2}) of rain, based on the GMMF simulations for 1 - 7 January 2007.

328 **3.3 Rain radiative effect at the CRM scale**

329 While rain may not have a large impact on the global mean radiation budget, this does
 330 not mean that the RRE never reaches values that are sufficiently large and occur sufficiently
 331 often to systematically influence the evolution of a LSAM. To investigate the range of RRE,
 332 Figure 5 shows the normalized frequency distribution of LW and SW RRE at the TOA, sur-
 333 face and in-atmosphere at the CRM column scale (i.e. a grid box of ~ 4 km). The distribu-

334 tions are based on 1.0 W m^{-2} bins, and include only those points where rain occurs. In order
 335 to highlight the full range of RRE, we use a log-scale for the frequency (y-axis). For the SW,
 336 we include all daylight points, so that the spread in the distribution is partially due to varia-
 337 tion in solar zenith angles.

338 The largest magnitude LW RRE values in Figure 5 are approximately 100 times larger
 339 than both the global mean values (see Table 1) and the mean RRE when rain occurs (see the
 340 numbers in the legends in Figure 5). We can see that LW RRE values at TOA, surface and
 341 in-atmosphere can all be either positive or negative; the cancellation between positive and
 342 negative RREs partly explains the small global mean RREs. Recall that *Savijärvi and Räisä-*
 343 *nen* [1998], reported a LW surface RRE of 24 W m^{-2} for a cloud with base at 3 km and a sur-
 344 face rain rate of 100 mm h^{-1} . Figure 5c shows that LW RREs of this magnitude are possible
 345 but rare (occurring in approximately one in a hundred thousand rainy columns). Under sim-
 346 ilar conditions (i.e. cloud base height of at least 3000 m and rain rate of at least 100 mm h^{-1})
 347 our calculations give a mean surface LW RRE of 14.8 W m^{-2} , which is considerably smaller
 348 than the value reported by *Savijärvi and Räisänen* [1998]. This is to be expected as *Savijärvi*
 349 *and Räisänen* [1998] point out that their estimates are likely to be too large due to an unre-
 350 alistically dry atmosphere below cloud base. Even more moderate LW surface RREs of 10
 351 W m^{-2} or greater are infrequent, occurring in only 0.4 % of the rainy CRM columns.

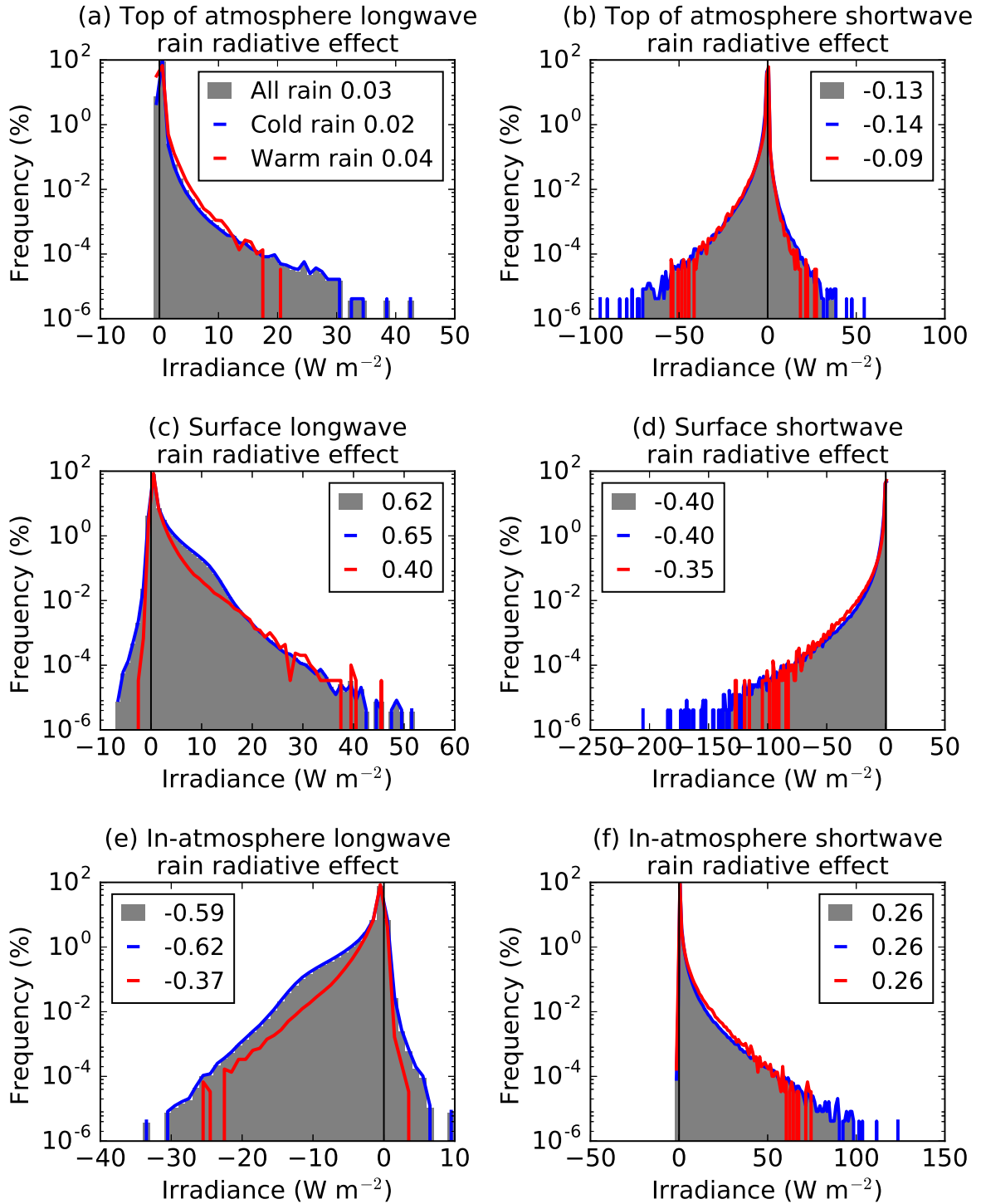
352 As mentioned earlier, the SW RRE distribution includes changes due to solar zenith
 353 angle; the largest RREs generally correspond to cases with small solar zenith angles, due to
 354 a larger amount of incoming solar radiation to be potentially absorbed or reflected. Similar
 355 to the LW, SW RRE values at TOA, surface and in-atmosphere can also all be either pos-
 356 itive or negative. However, positive surface SW RRE values are very rare (less than 0.01
 357 % of rainy daytime columns) and have very small magnitude (less than 0.5 W m^{-2}). Nega-
 358 tive in-atmosphere SW RRE are also rare (less than 0.05 % of rainy daytime columns) with
 359 small magnitude (less than 2.0 W m^{-2} in magnitude). *Savijärvi et al.* [1997] reported an in-
 360 atmosphere SW RRE of up to 65 W m^{-2} for an idealized heavily precipitating case with over-
 361 head sun. The distribution of RREs shown in Figure 5f shows that SW RREs of this magni-
 362 tude are possible but rare (occurring in less than 0.001 % of rainy columns). In our GMMF
 363 dataset, most of the heavily precipitating cases have large amounts of cloud water, and thus
 364 reflect large amounts of sunlight above the rainy layers, which reduces the amount of SW ra-
 365 diation that interacts with rain, making large RREs very unlikely. Even at the surface, where

366 the magnitude of the SW RRE is largest, only 0.8 % of rainy daytime cases have a RRE with
367 a magnitude as large as 10 W m^{-2} .

368 To investigate potential links between the RRE and rain formation processes, Figure 5
369 also shows separate distributions for warm and cold rain. Our method for separating warm
370 and cold rain is similar to *Mülmenstädt et al. [2015]*: when the rain-producing cloud contains
371 ice phase hydrometeors, we assume that the rain is due to ice phase processes and denote
372 this cold rain, otherwise warm rain is assumed. According to this separation, of the 19 % of
373 CRM columns that contain rain, 89 % are cold rain and 11 % are warm rain. Thus the total
374 rain radiative effect is dominated by cold rain and the mean RREs for all rain are much closer
375 to those for cold rain than those for warm rain (see legends in Figure 5).

376 There are clear differences between the RRE distributions for warm rain and cold rain.
377 Beginning with TOA LW irradiances, the cold rain mean RRE is slightly smaller than the
378 warm rain mean RRE (see legend for Figure 5a). This is because ice cloud is more likely to
379 be present above the rain in the cold rain cases, which absorbs and emits radiation at lower
380 temperatures and thereby reduces the impact of the rain on the TOA LW irradiances. In con-
381 trast, at the surface and in-atmosphere, the cold rain LW RRE is approximately 50 % larger
382 than the warm rain RRE. This is because the mean rain water path of 86.0 g m^{-2} for cold rain
383 is larger than that of 36.5 g m^{-2} for warm rain.

384 In the SW, the larger mean rain water path in cold rain columns also leads to a larger
385 mean RRE than for warm rain columns, both at the TOA and the surface (Figures 5b and 5d).
386 However, the mean SW in-atmosphere RRE has a similar magnitude for both cold rain and
387 warm rain (Figure 5f) due to two opposing factors. Cold rain columns have larger absorp-
388 tion by rain than warm rain columns. However, the reduction in absorption by cloud below
389 rain is also larger for cold rain columns than for warm rain columns. The larger increase in
390 absorption by rain for cold rain columns is caused by the larger mean rain water path and
391 droplet effective radius for cold rain columns. The larger decrease in absorption by cloud for
392 cold rain columns is because the single scattering albedo of cloud ice is smaller than that of
393 cloud liquid (Figure 3) and extinction by rain reduces the amount of radiation available to be
394 absorbed by any cloud below. Consequently, there is a larger decrease in cloud absorption
395 for cold rain where there is more likely to be ice cloud below the rain with a smaller single
396 scattering albedo.



397 **Figure 5.** Frequency distributions of RRE for 1-7 January and 1-7 July 2007 combined at TOA (top row),
 398 surface (middle) and in-atmosphere (bottom) for LW (left) and SW (right). Bin width is 1.0 W m^{-2} . The red
 399 line, blue line and gray bars show the distributions for warm, cold and all rain, respectively. Note that we only
 400 include grid boxes where rain is present in these distributions. The numbers in the legend show the means of
 401 the distributions.

4 What controls the rain radiative effect?

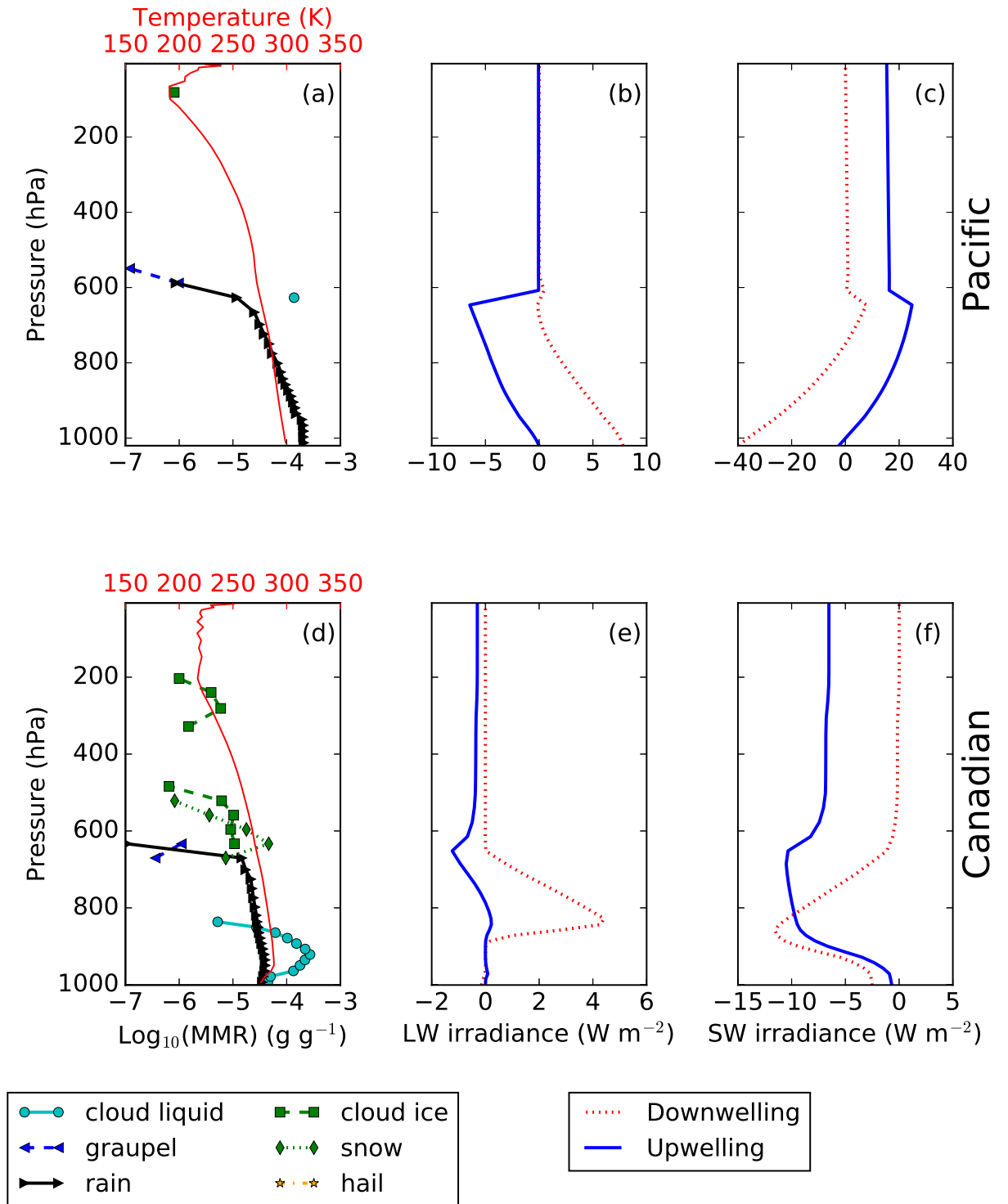
We have shown that, for individual CRM columns, the RRE can take a broad range of values, both positive and negative. In this section we identify the processes that determine the direction and magnitude of the RRE. Detailed analysis of two example hydrometeor and irradiance profiles with very different RREs is used to illustrate how these processes affect the RRE. Further analysis shows that the results from the case studies can be generalized to all rainy columns.

4.1 Case studies

The two case studies consist of individual CRM profiles and represent different vertical cloud structures: almost all the rain occurs below cloud base in the Pacific case; whereas about half the rainy layers are above the warm cloud in the Canadian case. Ice clouds are physically thicker with larger mass mixing ratios in the Canadian case. Together, these cases demonstrate that the rain radiative effect is determined not only by the rain water path itself, but also the relative water path with respect to other species, and the location of the rain layer. Details of these case studies are given in Table 2.

Location	Pacific ocean	Northern Canada
Latitude	8 °N	64 °N
Longitude	145 °W	85 °W
Date	6 Jan 2007	3 July 2007
Time (UTC)	01:00	15:00
Local solar time (approx.)	15:00	09:15
Surface rain rate (mm h ⁻¹)	3.9	0.2
SW insolation (W m ⁻²)	751	895
TOA LW RRE (W m ⁻²)	0.1	0.3
TOA SW RRE (W m ⁻²)	-15.4	6.5
Surface LW RRE (W m ⁻²)	7.8	-0.1
Surface SW RRE (W m ⁻²)	-37.5	-1.8

Table 2. Details of the two case studies used to illustrate the radiative effects of rain.



418 **Figure 6.** Examples of CRM columns with contrasting rain radiative effects. The top row shows the Pacific
 419 Ocean case and the bottom row shows the Northern Canada case. The left column shows mass mixing ratio
 420 (MMR) profiles for the six different hydrometeor species (black and grey) and the temperature profile (red).
 421 The middle column shows the corresponding all_hydro - no_rain LW profiles and the right column shows the
 422 corresponding all_hydro - no_rain SW profiles.

423 The Pacific Ocean is an example of the rain layer occurring below a liquid cloud layer.
424 This case consists of a CRM column located at the edge of a tropical cumulus congestus
425 cloud (Figure 6a), and has the larger rain mass mixing ratios of the two cases. Rain occurs
426 between 600 hPa (~ 5000 m) and the surface, falling from a ~ 1500 m thick layer consisting
427 of liquid cloud (occupying a single model layer ~ 500 m thick) and graupel (two model lay-
428 ers, each ~ 500 m thick), that sits just below the top of the congestus cloud in the neighboring
429 column. The cirrus cloud layer at ~ 80 hPa occupies only a single model layer and is inde-
430 pendent of the cumulus congestus cloud.

431 In the LW, the downwelling radiation emitted by the rain reaches the surface unim-
432 peded by cloud. Rain is warmer than the cloud above it and thus increases the downwelling
433 irradiance to the surface. In contrast, the liquid cloud above the rain absorbs and emits LW
434 radiation, and impedes the upwelling radiation emitted by the rain. As a result, the net irra-
435 diance at the surface increases, but the change at TOA is rather small, as shown in Figure 6b.
436 In the SW, by reflecting sunlight, rain increases the upwelling SW irradiance from the lowest
437 rainy layer to the TOA (Figure 6c), leading to a negative RRE at TOA. Reflection and ab-
438 sorption of sunlight also leads to a reduction in the downwelling irradiance from the highest
439 rain layer to the surface (Figure 6c), and thus a negative RRE at the surface. The RREs in
440 the Pacific case are particularly large due to the large rain mass mixing ratios, which lead to
441 larger extinction (Figure 3a) and small cloud water path, which means that large amounts of
442 SW radiation reach the rain layer.

443 In the Canadian case, the rain layer extends above the warm cloud. This case is a CRM
444 column located at the leading edge of a cold front (Figure 6d). The rain layer in this case
445 is a little shallower than the Pacific Ocean case, with smaller rain mass mixing ratios and
446 more complex cloud structure in the vertical. Snow and graupel fall from a convective anvil
447 at 500700 hPa levels, with the snow melting to form rain at ~ 625 hPa (~ 4000 m), which falls
448 through an optically thick warm cloud that extends from ~ 800 hPa (~ 1500 m) to the surface.
449 A temperature inversion, caused by the passage of the cold front, occurs between the surface
450 and ~ 950 hPa.

451 In the LW, the rain causes an increase in the downwelling LW irradiance above the
452 warm cloud top, but this is rapidly reduced below the warm cloud top, as emission by cloud
453 dominates over that from rain. As the liquid mass mixing ratio decreases near the surface,
454 the rain effect is no longer completely overshadowed by the cloud effect, though it remains

455 small. The temperature inversion means that rain emits radiation at colder temperatures than
456 the cloud above, so that rain reduces the downwelling LW irradiance and the net effect at the
457 surface is negative. Above the warm cloud, the reduction in upwelling irradiance due to rain
458 is overshadowed by absorption and emission at colder temperatures by the ice cloud above.
459 Consequently, the net RRE at the TOA is also very small. In the SW, the radiative effect of
460 rain above cloud is analogous to the radiative effect of an absorbing aerosol layer above cloud
461 [e.g. *Chand et al.*, 2009; *Wilcox*, 2012]. Since the absorbing rain layer is above the brighter
462 cloud layer, sunlight is absorbed that would otherwise be reflected by clouds, resulting in a
463 positive TOA SW RRE (see Table 2). For the downwelling SW irradiance, absorption and
464 reflection by rain cause a reduction in irradiance, which decreases with altitude below the
465 warm cloud top as the radiation that is absorbed and reflected by the rain would have been
466 reflected by the cloud anyway. As a result, the rain effect on the surface downwelling irradi-
467 ance is quite small.

468 4.2

469 The factors that have been identified as controlling the direction and magnitude of the
470 rain radiative effect in these case studies can be generalized to all rainy profiles, as shown in
471 Figure 7. This figure shows how the SW and LW RREs at both the TOA and surface change
472 as a function of the two main variables that we have identified as controlling the RRE. Note
473 that these variables depend on the particular RRE in question.

474 Focusing first on the LW, Figure 7(a) shows that the total water path above the rain top
475 plays a key role in limiting the LW TOA RRE. The RRE decreases rapidly as the total water
476 path above rain top increases, because as explained for the case studies, any hydrometeors
477 above the rain top overshadow the emission by rain. Figure 7(a) also shows that the LW TOA
478 RRE is affected by the difference in temperature between the rain top and the surface. The
479 magnitude of the LW TOA RRE increases as the magnitude of the difference increases. Gener-
480 ally, the rain top is cooler than the surface so the TOA LW RRE is positive, however temper-
481 ature inversions can lead to rain emitting at a higher temperature than the surface, leading to
482 a negative TOA LW RRE.

483 At the surface, Figure 7(c) shows that the LW RRE increases as the rain water path be-
484 low cloud base increases, because the extinction depends on the rain mass mixing ratio, but
485 as explained in the Canadian case, any emission by rain above the cloud base will be over-

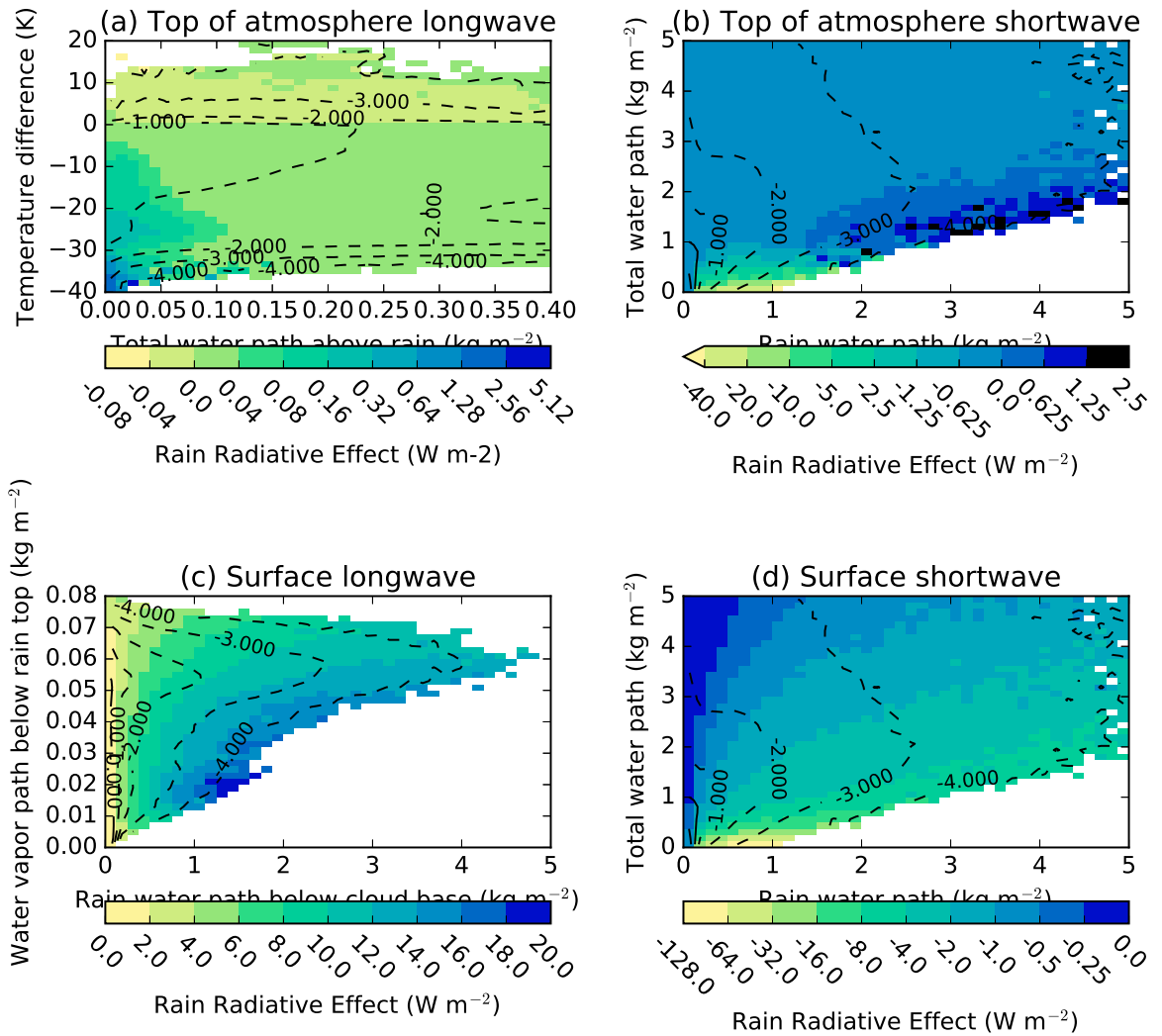
486 shadowed by emission from the cloud. The LW surface RRE decreases as the vapor water
487 path below the rain top increases, because emission by the vapor partly masks the emis-
488 sion by the rain. The rain water path below cloud base and vapor path below the rain top are
489 positively correlated, so that the radiative effect of an increase in one tends to be offset by the
490 radiative effect of an increase in the other. In general, as temperature decreases with height,
491 rain below cloud emits at higher temperatures than the cloud and increases the downwelling
492 LW radiation, leading to a positive RRE. However, if a temperature inversion near the surface
493 exists, the RRE can be negative as seen in the Canadian case.

494 Moving to the SW, Figure 7(b,d) shows both the surface and TOA RRE increase in
495 magnitude with increasing rain water path (as extinction by rain depends on the rain mass
496 mixing ratios) and decrease in magnitude as the total water path (excluding rain) increases
497 (because the amount of SW irradiance that is available for rain to reflect or absorb decreases).
498 The rain and total water path values are positively correlated, so again in general the effect of
499 an increase in one is offset by the effect of a decrease in the other. At the TOA, the SW RRE
500 is generally negative, with largest negative values when the total water path is small and the
501 rain water path is large. For total water path values larger than $\sim 1.5 \text{ kg m}^{-2}$, the mean RRE
502 for the largest rain water path values is positive, as these cases tend to coincide with rain oc-
503 ccurring above cloud base and absorbing radiation that would otherwise be reflected, as in the
504 Canadian case.

505 At the surface Figure 7(d) shows only negative values for the SW RRE. Analysis of the
506 positive values shown in Figure 5(d) shows that positive SW RREs only occur when the so-
507 lar zenith angle is very large, so that the albedo of both clouds and the surface is much larger
508 for direct radiation than diffuse radiation. In some of these cases, including small amounts of
509 rain can have little effect on the total downwelling SW irradiance, but lead to a large increase
510 in the fraction that is diffuse. As the albedo for diffuse radiation of the cloud or surface be-
511 low the rain is smaller than that for direct radiation, this can lead to an increase in the net
512 downwelling surface SW irradiance.

523 **5 Discussion**

524 The aim of this study is to quantify the radiative effect of rain (RRE). To our knowl-
525 edge, this study is the first time that the RRE has been quantified globally. This represents a



513 **Figure 7.** Rain radiative effect as a function of the state of the atmosphere, for all rainy CRM columns.
 514 Colors indicate the mean rain radiative effect in each X-Y bin (Note the non-linear scales used). Contour
 515 lines indicate the percentage of the total number of rainy columns in each bin. Bins with fewer than 10 sam-
 516 ples are not included. Panel (a) shows the mean TOA LW RRE for the given values of the total water path
 517 above the uppermost rainy layer and the temperature difference between the uppermost rainy layer and the
 518 surface. Panel (b) shows the mean SW TOA RRE for given values of the rain water path and the total water
 519 path (Which here includes vapor and all hydrometeors except rain), for lit points only. (c) shows the mean
 520 LW surface RRE for given values of the rain water path below cloud base (here cloud includes liquid, ice and
 521 snow) and the water vapor path below the uppermost rainy layer. Finally (d) shows the mean SW surface RRE
 522 for given values of the rain water path and the total water path, for lit points only.

526 key step in determining whether rain needs to be included in the radiative transfer calcula-
527 tions applied in numerical weather prediction (NWP) and climate models.

528 From a global mean perspective, the RRE is very small, being less than 0.2 W m^{-2}
529 for both SW and LW irradiances at the surface, TOA and in-atmosphere. These mean val-
530 ues are a fraction of the accuracy with which we can measure global mean irradiances [e.g.
531 *Stephens et al.*, 2012] and consequently, from a global mean perspective, the RRE can be re-
532 garded as negligible. Averaging over a single week, at the GMMF gridbox scale, the RRE
533 is largest for downwelling LW irradiance at the surface along the ITCZ, but remains less
534 than 4 W m^{-2} . These largest RRE values are smaller than both the uncertainty in both the
535 SW and LW global mean cloud radiative effects [e.g. *Stephens et al.*, 2012] and typical zonal
536 mean TOA radiation errors seen in climate models [e.g. *Dolinar et al.*, 2014]. Moreover, the
537 missing RRE can only explain a very small fraction of the persistent large (greater than 20
538 W m^{-2}) radiation errors seen in heavily precipitating regions in LSAMs.

539 At finer temporal and spatial scales, the RRE may be significant. At the finest scales
540 available from the GMMF (i.e. the CRM column scale), the magnitude of the LW RRE can
541 exceed 30 W m^{-2} at the surface, top of atmosphere and in-atmosphere. For small solar zenith
542 angles, the SW RRE can be even larger than this. Yet large RRE values are infrequent. For
543 the LW surface RRE, less than 0.1 % of the CRM columns have a RRE value larger than
544 10 W m^{-2} . Large RRE is more common for cold rain than warm rain events, primarily due
545 to larger rain water path values for cold rain. The LW surface RRE exceeds 10 W m^{-2} for
546 0.47 % of CRM columns identified as cold rain and 0.13 % of those identified as warm rain.
547 The RRE can be either positive or negative and the magnitude and direction depend on the
548 vertical location with respect to any other hydrometeors, the properties of the surface, and in
549 the LW the emission temperature of the rain and any other hydrometeors.

550 The calculations presented in this study were based on the assumption that the rain is
551 in thermal equilibrium with the ambient air. In reality, evaporative cooling and falling from
552 higher cooler altitudes may result in rain droplets that are cooler than the ambient air. Based
553 on theoretical calculations and assuming a constant lapse rate *Best* [1952] showed that evapo-
554 rative cooling has a larger effect, except in the case of very large rain droplets. He found that
555 rain droplets are up to 12.89 K cooler than the ambient temperature for a relative humidity
556 of 40 % and an ambient temperature of 314 K. This corresponds to a 15 % decrease in the
557 LW irradiance emitted by rain. However, for larger humidities, which generally coincide with

558 rain, the temperature difference is much smaller, being less than 1 K at 95 % relative humid-
559 ity, which corresponds to a decrease in the LW irradiance emitted by rain of less than 1 %.

560 Judging whether the exclusion of the rain radiative effect may negatively impact the
561 evolution of a LSAM requires comparison of simulations where the RRE is and is not in-
562 cluded interactively in that LSAM. However, previous studies have shown that LSAM simu-
563 lations are rather insensitive to radiative errors of a much larger magnitude that do not persist
564 in space or time [e.g. *Barker et al.*, 2008; *Hill et al.*, 2011; *Bozzo et al.*, 2014]. Moreover,
565 given the transient nature of the RRE it seems highly unlikely to have a systematic effect on
566 current LSAMs. Even when it is large the RRE is likely to be dwarfed by latent heating; for
567 approximately 88 % of CRM columns with a net downwelling surface LW RRE of at least
568 1.0 W m^{-2} , the surface latent heating is at least 10 times larger.

569 However, this study showed that at small scales the rain radiative effects can be quite
570 large. Thus it seems likely that at finer resolutions, the impact of the RRE on the realism of
571 the simulation will increase. At high resolution, orographic enhancement of precipitation
572 could lead to longer lasting large RREs at a fixed location. On this basis, the RRE is most
573 likely to be significant for regional NWP models. Moreover, while this study indicates that
574 excluding rain from LSAM radiative transfer calculations is unlikely to lead to large errors in
575 models, it does still lead to errors and there is no reason not to include rain in LSAM radia-
576 tive transfer calculations if the model already carries the required variables.

577 **Acknowledgments**

578 The research leading to this publication has received funding from the European Union 7th
579 Framework Programme (FP7/2007-2013) under grant agreement 603502 (EU project DAC-
580 CIWA: Dynamics-Aerosol-Chemistry-Cloud Interactions in West Africa). The authors would
581 like to thank Adrian Hill for providing data and assistance for some precursor calculations of
582 the rain radiative effect. The GMMF model outputs used in this study are available through
583 NASA Cloud Library Data Portal (<https://portal.nccs.nasa.gov/cloudlibrary/>) upon request
584 from Jiun-dar.chern-1@nasa.gov. The SOCRATES radiative transfer code including the
585 modifications required to both derive single scattering properties of rain, graupel and hail
586 and to calculate their broadband radiative effects is available from the Met Office Science
587 Repository Service ([https://code.metoffice.gov.uk/trac/socrates/browser#](https://code.metoffice.gov.uk/trac/socrates/browser#main/branches/dev/peterhill/r58_hydrometeor_rad_effects)
588 [main/branches/dev/peterhill/r58_hydrometeor_rad_effects](https://code.metoffice.gov.uk/trac/socrates/browser#main/branches/dev/peterhill/r58_hydrometeor_rad_effects)). Results from the

589 calculations are freely available from the University of Reading Research Data Archive at
 590 <http://researchdata.reading.ac.uk/id/eprint/174>.

591 **A: Rain, graupel and hail single scattering properties parametrizations**

592 Extinction (β), single scattering albedo (ω), and asymmetry (g) for rain, graupel
 593 and hail are calculated using Mie theory as described in section 2.2. A least squares method
 594 is then used to parametrize this dataset using the following simple equations proposed by
 595 *Slingo and Schrecker* [1982].

$$\beta = q \cdot \left(A + \frac{B}{r_e} \right) \quad (\text{A.1})$$

$$1 - \omega = C + D \cdot r_e \quad (\text{A.2})$$

$$g = E + F \cdot r_e \quad (\text{A.3})$$

596 where A, B, C, D, E, F are coefficients determined by performing the least square fitting with
 597 values given in the following tables. Tables A.1, A.2, and A.3 show the values for the coef-
 598 ficients used in the parametrization of the single scattering properties of rain, graupel, and
 599 hail, respectively, for each of the 6 SW and 9 LW bands.

603 **References**

- 604 Baran, A. J., and L.-C. Labonnote (2007), A self-consistent scattering model for cirrus. I:
 605 The solar region, *Quarterly Journal of the Royal Meteorological Society*, 133(629), 1899–
 606 1912.
- 607 Baran, A. J., P. Field, K. Furtado, J. Manners, and A. Smith (2013), A new high- and low-
 608 frequency scattering parameterization for cirrus and its impact on a high-resolution numer-
 609 ical weather prediction model, *AIP Conf. Proc.*, 1531, 716–719.
- 610 Barker, H. W., J. N. S. Cole, J.-J. Morcrette, R. Pincus, P. R  lais  lanen, K. von Salzen, and
 611 P. A. Vaillancourt (2008), The Monte Carlo Independent Column Approximation: An as-
 612 sessment using several global atmospheric models, *Q. J. Roy. Meteorol. Soc.*, 134, 1463–
 613 1478.

Wavelength (m)	A	B	C	D	E	F
Shortwave Bands						
$2.00 \times 10^{-7} - 3.20 \times 10^{-7}$	-9.9833×10^{-4}	1.5035×10^{-3}	3.1562×10^{-5}	2.0421×10^0	8.7270×10^{-1}	4.2819×10^{-1}
$3.20 \times 10^{-7} - 6.90 \times 10^{-7}$	-1.4670×10^{-3}	1.5052×10^{-3}	6.6121×10^{-7}	1.2662×10^{-1}	8.8226×10^{-1}	1.3567×10^{-1}
$3.20 \times 10^{-7} - 6.90 \times 10^{-7}$	-1.4670×10^{-3}	1.5052×10^{-3}	6.6121×10^{-7}	1.2662×10^{-1}	8.8226×10^{-1}	1.3567×10^{-1}
$6.90 \times 10^{-7} - 1.19 \times 10^{-6}$	-2.3649×10^{-3}	1.5083×10^{-3}	1.9200×10^{-3}	1.2149×10^1	8.8564×10^{-1}	1.9942×10^0
$1.19 \times 10^{-6} - 2.38 \times 10^{-6}$	-3.5276×10^{-3}	1.5124×10^{-3}	2.6483×10^{-1}	4.5330×10^1	9.2606×10^{-1}	9.8247×10^0
$2.38 \times 10^{-6} - 1.00 \times 10^{-5}$	-6.8263×10^{-3}	1.5238×10^{-3}	4.6536×10^{-1}	3.7050×10^{-1}	9.7142×10^{-1}	1.0231×10^{-1}
Longwave Bands						
$3.34 \times 10^{-6} - 6.67 \times 10^{-6}$	-7.1358×10^{-3}	1.5248×10^{-3}	4.6489×10^{-1}	1.4904×10^{-1}	9.7039×10^{-1}	5.3054×10^{-2}
$6.67 \times 10^{-6} - 7.52 \times 10^{-6}$	-9.4553×10^{-3}	1.5329×10^{-3}	4.6797×10^{-1}	-2.5385×10^{-1}	9.7361×10^{-1}	1.8214×10^{-2}
$7.52 \times 10^{-6} - 8.33 \times 10^{-6}$	-1.0169×10^{-2}	1.5354×10^{-3}	4.6977×10^{-1}	-3.4776×10^{-1}	9.7568×10^{-1}	3.6619×10^{-2}
$8.33 \times 10^{-6} - 1.25 \times 10^{-5}$	-1.0732×10^{-2}	1.5383×10^{-3}	4.7445×10^{-1}	-6.7541×10^{-1}	9.8106×10^{-1}	8.0455×10^{-2}
$8.93 \times 10^{-6} - 1.01 \times 10^{-5}$	-1.1270×10^{-2}	1.5394×10^{-3}	4.7472×10^{-1}	-5.8781×10^{-1}	9.8107×10^{-1}	7.2116×10^{-2}
$1.25 \times 10^{-5} - 1.82 \times 10^{-5}$	-1.3333×10^{-2}	1.5479×10^{-3}	4.5170×10^{-1}	-6.6916×10^{-1}	9.5177×10^{-1}	1.0014×10^{-2}
$1.33 \times 10^{-5} - 1.69 \times 10^{-5}$	-1.3676×10^{-2}	1.5489×10^{-3}	4.4820×10^{-1}	-6.2890×10^{-1}	9.4747×10^{-1}	-1.8311×10^{-2}
$1.82 \times 10^{-5} - 2.50 \times 10^{-5}$	-1.8573×10^{-2}	1.5656×10^{-3}	4.4060×10^{-1}	-1.1709×10^0	9.3037×10^{-1}	-4.1360×10^{-2}
$2.50 \times 10^{-5} - 1.00 \times 10^{-2}$	-3.9201×10^{-2}	1.6537×10^{-3}	4.3890×10^{-1}	-6.5461×10^0	8.8105×10^{-1}	3.6852×10^0

600

Table A.1. Parameters derived for the parametrization of the single scattering properties of rain.

Wavelength (m)	A	B	C	D	E	F
Shortwave Bands						
$2.00 \times 10^{-7} - 3.20 \times 10^{-7}$	-3.1038×10^{-3}	5.0115×10^{-3}	1.4616×10^{-6}	4.2090×10^{-1}	8.7621×10^{-1}	1.2914×10^{-1}
$3.20 \times 10^{-7} - 6.90 \times 10^{-7}$	-4.7369×10^{-3}	5.0173×10^{-3}	3.8750×10^{-7}	9.4962×10^{-2}	8.8956×10^{-1}	1.2846×10^{-1}
$3.20 \times 10^{-7} - 6.90 \times 10^{-7}$	-4.7369×10^{-3}	5.0173×10^{-3}	3.8750×10^{-7}	9.4962×10^{-2}	8.8956×10^{-1}	1.2846×10^{-1}
$6.90 \times 10^{-7} - 1.19 \times 10^{-6}$	-7.4355×10^{-3}	5.0273×10^{-3}	6.1986×10^{-4}	7.4361×10^0	8.9428×10^{-1}	1.2573×10^0
$1.19 \times 10^{-6} - 2.38 \times 10^{-6}$	-1.1152×10^{-2}	5.0407×10^{-3}	2.7466×10^{-1}	3.9109×10^1	9.3372×10^{-1}	8.0019×10^0
$2.38 \times 10^{-6} - 1.00 \times 10^{-5}$	-2.0956×10^{-2}	5.0766×10^{-3}	4.6132×10^{-1}	1.1681×10^0	9.6803×10^{-1}	2.1389×10^{-1}
Longwave Bands						
$3.34 \times 10^{-6} - 6.67 \times 10^{-6}$	-2.2118×10^{-2}	5.0806×10^{-3}	4.6377×10^{-1}	-1.6486×10^{-3}	9.6825×10^{-1}	-7.6178×10^{-3}
$6.67 \times 10^{-6} - 7.52 \times 10^{-6}$	-2.9064×10^{-2}	5.1061×10^{-3}	4.6716×10^{-1}	-2.5538×10^{-1}	9.7254×10^{-1}	1.0740×10^{-2}
$7.52 \times 10^{-6} - 8.33 \times 10^{-6}$	-3.1406×10^{-2}	5.1146×10^{-3}	4.6806×10^{-1}	-3.3497×10^{-1}	9.7344×10^{-1}	2.5193×10^{-2}
$8.33 \times 10^{-6} - 1.25 \times 10^{-5}$	-3.3325×10^{-2}	5.1243×10^{-3}	4.6418×10^{-1}	-4.9849×10^{-1}	9.6846×10^{-1}	3.4249×10^{-2}
$8.93 \times 10^{-6} - 1.01 \times 10^{-5}$	-3.4940×10^{-2}	5.1277×10^{-3}	4.7456×10^{-1}	-5.8789×10^{-1}	9.8077×10^{-1}	7.1164×10^{-2}
$1.25 \times 10^{-5} - 1.82 \times 10^{-5}$	-4.6831×10^{-2}	5.1717×10^{-3}	4.4659×10^{-1}	-7.2908×10^{-1}	9.4073×10^{-1}	-4.4234×10^{-2}
$1.33 \times 10^{-5} - 1.69 \times 10^{-5}$	-4.7467×10^{-2}	5.1738×10^{-3}	4.4677×10^{-1}	-7.5554×10^{-1}	9.3977×10^{-1}	-4.8595×10^{-2}
$1.82 \times 10^{-5} - 2.50 \times 10^{-5}$	-6.1003×10^{-2}	5.2223×10^{-3}	4.5790×10^{-1}	-1.134×10^0	9.5445×10^{-1}	2.4309×10^{-1}
$2.50 \times 10^{-5} - 1.00 \times 10^{-2}$	1.6860×10^{-1}	5.0053×10^{-3}	-8.1138×10^0	7.1646×10^2	-1.6628×10^{-2}	9.5776×10^1

601

Table A.2. Parameters derived for the parametrization of the single scattering properties of graupel.

Wavelength (m)	A	B	C	D	E	F
Shortwave Bands						
$2.00 \times 10^{-7} - 3.20 \times 10^{-7}$	-4.3479×10^{-4}	1.6689×10^{-3}	-7.0683×10^{-6}	4.2411×10^{-1}	8.7626×10^{-1}	1.0713×10^{-1}
$3.20 \times 10^{-7} - 6.90 \times 10^{-7}$	-7.4316×10^{-4}	1.6703×10^{-3}	-1.4956×10^{-6}	9.5675×10^{-2}	8.8971×10^{-1}	7.1167×10^{-2}
$3.20 \times 10^{-7} - 6.90 \times 10^{-7}$	-7.4316×10^{-4}	1.6703×10^{-3}	-1.4956×10^{-6}	9.5675×10^{-2}	8.8971×10^{-1}	7.1167×10^{-2}
$6.90 \times 10^{-7} - 1.19 \times 10^{-6}$	-1.1712×10^{-3}	1.6724×10^{-3}	7.8949×10^{-4}	7.3683×10^0	8.9447×10^{-1}	1.1832×10^0
$1.19 \times 10^{-6} - 2.38 \times 10^{-6}$	-1.4505×10^{-3}	1.6744×10^{-3}	3.0588×10^{-1}	2.6963×10^1	9.3851×10^{-1}	6.1403×10^0
$2.38 \times 10^{-6} - 1.00 \times 10^{-5}$	-2.7420×10^{-3}	1.6813×10^{-3}	4.6355×10^{-1}	3.0059×10^{-1}	9.6853×10^{-1}	1.9572×10^{-2}
Longwave Bands						
$3.34 \times 10^{-6} - 6.67 \times 10^{-6}$	-2.8780×10^{-3}	1.6820×10^{-3}	4.6356×10^{-1}	7.7907×10^{-2}	9.6831×10^{-1}	-2.8267×10^{-2}
$6.67 \times 10^{-6} - 7.52 \times 10^{-6}$	-3.7901×10^{-3}	1.6869×10^{-3}	4.6652×10^{-1}	-7.5130×10^{-3}	9.7261×10^{-1}	-1.5754×10^{-2}
$7.52 \times 10^{-6} - 8.33 \times 10^{-6}$	-4.0923×10^{-3}	1.6886×10^{-3}	4.6731×10^{-1}	-4.3151×10^{-2}	9.7353×10^{-1}	-1.0611×10^{-2}
$8.33 \times 10^{-6} - 1.25 \times 10^{-5}$	-4.5065×10^{-3}	1.6912×10^{-3}	4.6316×10^{-1}	-1.0280×10^{-1}	9.6859×10^{-1}	-1.4137×10^{-2}
$8.93 \times 10^{-6} - 1.01 \times 10^{-5}$	-4.5538×10^{-3}	1.6911×10^{-3}	4.7348×10^{-1}	-1.6872×10^{-1}	9.8092×10^{-1}	1.3592×10^{-2}
$1.25 \times 10^{-5} - 1.82 \times 10^{-5}$	-6.1634×10^{-3}	1.6998×10^{-3}	4.4522×10^{-1}	-1.9536×10^{-1}	9.4084×10^{-1}	-8.7242×10^{-2}
$1.33 \times 10^{-5} - 1.69 \times 10^{-5}$	-6.2296×10^{-3}	1.7001×10^{-3}	4.4537×10^{-1}	-2.1024×10^{-1}	9.3987×10^{-1}	-8.9204×10^{-2}
$1.82 \times 10^{-5} - 2.50 \times 10^{-5}$	-7.9212×10^{-3}	1.7091×10^{-3}	4.5621×10^{-1}	-4.7367×10^{-1}	9.5506×10^{-1}	2.3164×10^{-3}
$2.50 \times 10^{-5} - 1.00 \times 10^{-2}$	1.0351×10^{-1}	1.5477×10^{-3}	-1.0529×10^1	1.6562×10^3	-1.1768×10^{-1}	1.3509×10^2

602

Table A.3. Parameters derived for the parametrization of the single scattering properties of hail.

- 614 Beard, K. V., V. Bringi, and M. Thurai (2010), A new understanding of raindrop shape, *At-*
 615 *mospheric Research*, 97(4), 396–415.
- 616 Best, A. C. (1952), The evaporation of raindrops, *Quarterly Journal of the Royal Meteorolo-*
 617 *gical Society*, 78(336), 200–225.
- 618 Bozzo, A., R. Pincus, I. Sandu, and J.-J. Morcrette (2014), Impact of a spectral sampling
 619 technique for radiation on ECMWF weather forecasts, *J. Adv. Model. Earth Syst.*, 6(4),
 620 1288–1300.
- 621 Calisto, M., D. Folini, M. Wild, and L. Bengtsson (2014), Cloud radiative forcing intercom-
 622 parison between fully coupled CMIP5 models and CERES satellite data, *Annales Geo-*
 623 *physicae*, 32(7), 793–807.
- 624 Chand, D., R. Wood, T. L. Anderson, S. K. Satheesh, and R. J. Charlson (2009), Satellite-
 625 derived direct radiative effect of aerosols dependent on cloud cover, *Nature Geoscience*,
 626 2(3), 181–184.
- 627 Chen, Y.-W., T. Seiki, C. Kodama, M. Satoh, and A. T. Noda (2018), Impact of Precipitating
 628 Ice Hydrometeors on Longwave Radiative Effect Estimated by a Global Cloud-System
 629 Resolving Model, *Journal of Advances in Modeling Earth Systems*, 10(2), 284–296.
- 630 Chern, J.-D., W.-K. Tao, S. E. Lang, T. Matsui, J.-L. F. Li, K. I. Mohr, G. M. Skofronick-
 631 Jackson, and C. D. Peters-Lidard (2016), Performance of the Goddard multiscale modeling
 632 framework with Goddard ice microphysical schemes, *Journal of Advances in Modeling*
 633 *Earth Systems*, 8(1), 66–95.
- 634 Cole, J. N. S., H. W. Barker, D. A. Randall, M. F. Khairoutdinov, and E. E. Clothiaux
 635 (2005a), Global consequences of interactions between clouds and radiation at scales un-
 636 resolved by global climate models, *Geophys. Res. Lett.*, 32(L06703).
- 637 Cole, J. N. S., H. W. Barker, W. O’Hirok, E. E. Clothiaux, M. F. Khairoutdinov, and D. A.
 638 Randall (2005b), Atmospheric radiative transfer through global arrays of 2D clouds, *Geo-*
 639 *physical Research Letters*, 32(L19817).
- 640 Dee, D. P., S. M. Uppala, A. J. Simmons, P. Berrisford, P. Poli, S. Kobayashi, U. Andrae,
 641 M. A. Balmaseda, G. B. and P. Bauer, P. Bechtold, A. C. M. Beljaars, L. van de Berg,
 642 J. Bidlot, N. Bormann, C. Delsol, R. Dragani, M. Fuentes, A. J. Geer, L. Haimberger, S. B.
 643 Healy, H. Hersbach, E. V. HÅşlm, L. Isaksen, P. KÅllberg, M. KÅhler, M. Matricardi,
 644 A. P. McNally, B. M. Monge-Sanz, J.-J. Morcrette, B.-K. Park, C. Peubey, P. de Rosnay,
 645 C. Tavolato, J.-N. ThÅpaut, and F. Vitart (2011), The ERA-Interim reanalysis: configura-
 646 tion and performance of the data assimilation system, *Q. J. Roy. Meteorol. Soc.*, 137(656),

- 647 553–597.
- 648 Dolinar, E. K., X. Dong, B. Xi, J. H. Jiang, and H. Su (2014), Evaluation of CMIP5 simu-
649 lated clouds and TOA radiation budgets using NASA satellite observations, *Climate Dy-*
650 *namics*, 44(7-8), 2229–2247.
- 651 Downing, H. D., and D. Williams (1975), Optical constants of water in the infrared, *Journal*
652 *of Geophysical Research*, 80(12), 1656–1661.
- 653 Edwards, J. M., and A. Slingo (1996), Studies with a flexible new radiation code. 1: Choos-
654 ing a configuration for a large-scale model, *Q. J. Roy. Meteorol. Soc.*, 122, 690–719.
- 655 Fu, Q., S. K. Krueger, and K. N. Liou (1995), Interactions of Radiation and Convection in
656 Simulated Tropical Cloud Clusters, *Journal of the Atmospheric Sciences*, 52(9), 1310–
657 1328.
- 658 Hale, G. M., and M. R. Querry (1973), Optical Constants of Water in the 200-nm to 200-
659 $\hat{\text{A}}\text{m}$ Wavelength Region, *Appl. Opt.*, 12(3), 555–563.
- 660 Hill, P. G., J. Manners, and J. C. Petch (2011), Reducing noise associated with the Monte
661 Carlo Independent Column Approximation for weather forecasting models, *Q. J. Roy. Me-*
662 *eteorol. Soc.*, 137(654), 219–228.
- 663 Hong, Y., G. Liu, and J.-L. F. Li (2016), Assessing the Radiative Effects of Global Ice
664 Clouds Based on CloudSat and CALIPSO Measurements, *Journal of Climate*, 29(21),
665 7651–7674.
- 666 Iguchi, T., T. Kozu, R. Meneghini, J. Awaka, and K. Okamoto (2000), Rain-Profiling Algo-
667 rithm for the TRMM Precipitation Radar, *Journal of Applied Meteorology*, 39(12), 2038–
668 2052.
- 669 Jiang, H., and W. R. Cotton (2000), Large Eddy Simulation of Shallow Cumulus Convection
670 during BOMEX: Sensitivity to Microphysics and Radiation, *Journal of the Atmospheric*
671 *Sciences*, 57(4), 582–594.
- 672 Kou, L., D. Labrie, and P. Chylek (1993), Refractive indices of water and ice in the 0.65- to
673 25- μm spectral range, *Appl. Opt.*, 32(19), 3531–3540.
- 674 Lang, S. E., W.-K. Tao, J.-D. Chern, D. Wu, and X. Li (2014), Benefits of a Fourth Ice Class
675 in the Simulated Radar Reflectivities of Convective Systems Using a Bulk Microphysics
676 Scheme, *Journal of the Atmospheric Sciences*, 71(10), 3583–3612.
- 677 Lebsock, M. D., and T. S. L'Ecuyer (2011), The retrieval of warm rain from CloudSat, *J.*
678 *Geophys. Res.*, 116(D20).

- 679 L'Ecuyer, T. S., and G. L. Stephens (2002), An Estimation-Based Precipitation Retrieval Al-
680 gorithm for Attenuating Radars, *Journal of Applied Meteorology*, *41*(3), 272–285.
- 681 Li, J.-L. F., D. E. Waliser, G. Stephens, S. Lee, T. L'Ecuyer, S. Kato, N. Loeb, and H.-Y.
682 Ma (2013), Characterizing and understanding radiation budget biases in CMIP3/CMIP5
683 GCMs, contemporary GCM, and reanalysis, *Journal of Geophysical Research: Atmo-*
684 *spheres*, *118*(15), 8166–8184.
- 685 Li, J.-L. F., W.-L. Lee, D. E. Waliser, J. David Neelin, J. P. Stachnik, and T. Lee (2014a),
686 Cloud-precipitation-radiation-dynamics interaction in global climate models: A snow
687 and radiation interaction sensitivity experiment, *Journal of Geophysical Research: At-*
688 *mospheres*, *119*(7), 3809–3824.
- 689 Li, J.-L. F., R. M. Forbes, D. E. Waliser, G. Stephens, and S. Lee (2014b), Characterizing the
690 radiative impacts of precipitating snow in the ECMWF Integrated Forecast System global
691 model, *Journal of Geophysical Research: Atmospheres*, *119*(16), 9626–9637.
- 692 Li, J.-L. F., W.-L. Lee, J.-Y. Yu, G. Hulley, E. Fetzer, Y.-C. Chen, and Y.-H. Wang (2016a),
693 The impacts of precipitating hydrometeors radiative effects on land surface temperature
694 in contemporary GCMs using satellite observations, *Journal of Geophysical Research:*
695 *Atmospheres*, *121*(1), 67–79.
- 696 Li, J.-L. F., W.-L. Lee, D. Waliser, Y.-H. Wang, J.-Y. Yu, X. Jiang, T. L'Ecuyer, Y.-C. Chen,
697 T. Kubar, E. Fetzer, and M. Mahakur (2016b), Considering the radiative effects of snow
698 on tropical Pacific Ocean radiative heating profiles in contemporary GCMs using A-Train
699 observations, *Journal of Geophysical Research: Atmospheres*, *121*(4), 1621–1636.
- 700 Li, J.-L. F., D. E. Waliser, G. Stephens, and S. Lee (2016c), Characterizing and Understand-
701 ing Cloud Ice and Radiation Budget Biases in Global Climate Models and Reanalysis,
702 *Meteorological Monographs*, *56*, 13.1–13.20.
- 703 Ma, Q., K. Wang, and M. Wild (2014), Evaluations of atmospheric downward longwave ra-
704 diation from 44 coupled general circulation models of CMIP5, *Journal of Geophysical*
705 *Research: Atmospheres*, *119*(8), 4486–4497.
- 706 Marshall, J. S., and W. M. K. Palmer (1948), THE DISTRIBUTION OF RAINDROPS
707 WITH SIZE, *Journal of Meteorology*, *5*(4), 165–166.
- 708 Mülmenstädt, J., O. Sourdeval, J. Delanoë, and J. Quaas (2015), Frequency of occurrence of
709 rain from liquid-, mixed-, and ice-phase clouds derived from A-Train satellite retrievals,
710 *Geophys. Res. Lett.*, *42*(15), 6502–6509.

- 711 Petch, J. C. (1998), Improved radiative transfer calculations from information provided by
712 bulk microphysical schemes, *J. Atmos. Sci.*, 55(10), 1846–1858.
- 713 Phillips, V. T. J., and L. J. Donner (2006), Cloud microphysics, radiation and vertical veloc-
714 ities in two- and three-dimensional simulations of deep convection, *Quarterly Journal of*
715 *the Royal Meteorological Society*, 132(621C), 3011–3033.
- 716 Reynolds, R. W., T. M. Smith, C. Liu, D. B. Chelton, K. S. Casey, and M. G. Schlax (2007),
717 Daily High-Resolution-Blended Analyses for Sea Surface Temperature, *Journal of Cli-*
718 *mate*, 20(22), 5473–5496.
- 719 Savijärvi, H., and P. Räisänen (1998), Long-wave optical properties of water clouds and rain,
720 *Tellus A: Dynamic Meteorology and Oceanography*, 50(1), 1–11.
- 721 Savijärvi, H., A. Arola, and P. Räisänen (1997), Short-wave optical properties of precipitat-
722 ing water clouds, *Quarterly Journal of the Royal Meteorological Society*, 123(540), 883–
723 899.
- 724 Slingo, A., and H. M. Schrecker (1982), On the shortwave radiative properties of stratiform
725 water clouds, *Q. J. Roy. Meteorol. Soc.*, 108(456), 407–426.
- 726 Stephens, G. L., J. Li, M. Wild, C. A. Clayson, N. Loeb, S. Kato, T. L'Ecuyer, P. W. Stack-
727 house, M. Lebsock, and T. Andrews (2012), An update on Earth's energy balance in light
728 of the latest global observations, *Nature Geosci.*, 5(10), 691–696.
- 729 Tang, G., P. Yang, P. G. Stegmann, R. L. Panetta, L. Tsang, and B. Johnson (2017), Effect
730 of Particle Shape, Density, and Inhomogeneity on the Microwave Optical Properties of
731 Graupel and Hailstones, *IEEE Transactions on Geoscience and Remote Sensing*, 55(11),
732 6366–6378.
- 733 Tao, W.-K., J. Simpson, D. Baker, S. Braun, M.-D. Chou, B. Ferrier, D. Johnson, A. Khain,
734 S. Lang, B. Lynn, C.-L. Shie, D. Starr, C.-H. Sui, Y. Wang, and P. Wetzell (2003), Micro-
735 physics, radiation and surface processes in the Goddard Cumulus Ensemble (GCE) model,
736 *Meteorology and Atmospheric Physics*, 82(1-4), 97–137.
- 737 Tao, W.-K., W. Lau, J. Simpson, J.-D. Chern, R. Atlas, D. Randall, M. Khairoutdinov, J.-
738 L. Li, D. E. Waliser, J. Jiang, A. Hou, X. Lin, and C. Peters-Lidard (2009), A Multiscale
739 Modeling System: Developments, Applications, and Critical Issues, *Bulletin of the Ameri-*
740 *can Meteorological Society*, 90(4), 515–534.
- 741 Tao, W.-K., S. Lang, X. Zeng, X. Li, T. Matsui, K. Mohr, D. Posselt, J. Chern, C. Peters-
742 Lidard, P. M. Norris, I.-S. Kang, I. Choi, A. Hou, K.-M. Lau, and Y.-M. Yang (2014), The
743 Goddard Cumulus Ensemble model (GCE): Improvements and applications for studying

- 744 precipitation processes, *Atmospheric Research*, *143*, 392–424.
- 745 Tao, W.-K., D. Wu, S. Lang, J.-D. Chern, C. Peters-Lidard, A. Fridlind, and T. Matsui
746 (2016), High-resolution NU-WRF simulations of a deep convective-precipitation system
747 during MC3E: Further improvements and comparisons between Goddard microphysics
748 schemes and observations, *Journal of Geophysical Research: Atmospheres*, *121*(3), 1278–
749 1305.
- 750 Waliser, D. E., J.-L. F. Li, T. S. L'Ecuyer, and W.-T. Chen (2011), The impact of precipitating
751 ice and snow on the radiation balance in global climate models, *Geophys. Res. Lett.*, *38*(6).
- 752 Warren, S. G. (1984), Optical constants of ice from the ultraviolet to the microwave, *Appl.*
753 *Opt.*, *23*(8), 1206–1225.
- 754 Wilcox, E. M. (2012), Direct and semi-direct radiative forcing of smoke aerosols over clouds,
755 *Atmospheric Chemistry and Physics*, *12*(1), 139–149.
- 756 Wild, M., D. Folini, M. Z. Hakuba, C. Schär, S. I. Seneviratne, S. Kato, D. Rutan, C. Am-
757 mann, E. F. Wood, and G. König-Langlo (2014), The energy balance over land and
758 oceans: an assessment based on direct observations and CMIP5 climate models, *Climate*
759 *Dynamics*, *44*(11-12), 3393–3429.
- 760 Xu, K.-M., and D. A. Randall (1995), Impact of Interactive Radiative Transfer on the Macro-
761 scopic Behavior of Cumulus Ensembles. Part I: Radiation Parameterization and Sensitivity
762 Tests, *Journal of the Atmospheric Sciences*, *52*(7), 785–799.